Applied Energy 228 (2018) 1601–1617

Contents lists available at ScienceDirect

Applied Energy

journal homepage: www.elsevier.com/locate/apenergy

A test-validated prediction model of thermal contact resistance for Ti-6Al-4V alloy

Yan-Jun Dai[a], Jian-Jun Gou[b], Xing-Jie Ren[a], Fan Bai[a], Wen-Zhen Fang[a], Wen-Quan Tao[a,*]

[a] Key Laboratory of Thermo-Fluid Science and Engineering of MOE, School of Energy and Power Engineering, Xi'an Jiaotong University, Xi'an, Shaanxi 710049, China
[b] Shaanxi Aerospace Flight Vehicle Key Laboratory, School of Astronautics, Northwestern Polytechnical University, Xi'an 710072, China

HIGHLIGHTS

- Proposed a thermal contact resistance prediction model.
- Radiation effect whether to be considered is analyzed.
- The prediction model is experimentally validated.

ARTICLE INFO

Keywords:
Thermal contact resistance
Numerical simulation
Actual rough surfaces
Experimental measurement
Correlation

ABSTRACT

The precise prediction or test of thermal contact resistance is a key issue on increasing or decreasing thermal energy transmission efficiency between two solids. This paper raises a thermal contact resistance prediction model based on measuring actual surface topography under different loading pressures and different heating temperatures. The actual topography of contact surfaces is measured by a 3-D optical microscope named Bruker Contour GT-K. The contact surfaces are reconstructed with language Python according to the data of surface topography from the microscope and the numerical contact model is generated. Then the thermal contact resistance simulation is implemented with software ABAQUS. Based on the elastic-plastic constitutive equations and steady state heat conduction theory, finite element analysis of mechanical and heat transfer performance of the contact model is performed with ABAQUS in the light of sequential coupling method. The studied material pairs are Ti-6Al-4V—Ti-6Al-4V with three kinds of different interstitial material e.g., vacuum, air and conductive silicone grease. The effect of radiation on thermal contact resistance under air and vacuum atmosphere is further studied and analyzed. Besides, the solid thermal conductivity on thermal contact resistance is investigated. To verify the accuracy of the method, the simulated results from ABAQUS are compared with the experimental results of air gap with the same boundary conditions. The maximum deviation between simulation results and experimental results is 9.57% while 75% of the deviations are within 5%. A correlation of thermal contact conductance with the average contact surface temperature and loading pressure is proposed. The results show that this method has high precision to predict thermal contact resistance in the engineering application.

1. Introduction

Thermal contact conductance (TCC), which is the reciprocal of thermal contact resistance (TCR), has been utilized extensively in academics and industry, especially in the superconduction, cryogenics, nuclear industry, aircraft industry, spacecraft and satellites, microelectronics, nano-technologies, etc. [1]. Some applications, where a low value of the TCR is necessary. For example, cooling in electronic systems [2] and the fuel/can interface of a nuclear reactor [3]. Since the conduction through the contact interface is the first way to transfer the heat dissipated by the high power density chips, reducing the TCR becomes essential for the cooling technology development. The interfacial insert of appropriate material is adopted to minimise the thermal resistance of the metallic contacts [4]. The temperature difference between uranium dioxide fuel and the zircaloy sheath can reach several scores of degrees if the contact between them is poor. This can lead to overheating and potential melt down. On the other hand, there are several instances where a high value of TCR is desirable. In aerospace fields, the higher TCR is expected between the outer layer material and structure of aerodynamically heated supersonic flight vehicles. The

* Corresponding author.
E-mail address: wqtao@mail.xjtu.edu.cn (W.-Q. Tao).

https://doi.org/10.1016/j.apenergy.2018.06.134
Received 1 November 2017; Received in revised form 21 June 2018; Accepted 29 June 2018
Available online 18 July 2018
0306-2619/

higher TCR between the individual particles of a stationary packed bed can increase the effectiveness of the insulation. Therefore, during the past decades, numerous studies have been conducted to determine the TCR between various materials. A brief review will be conducted first for the experimental studies after the year of 2000 and followed by the theoretical considerations, prediction methods and models since 1974. In the experimental aspect, one dimensional steady state method is the most widely used method to measure TCR based on the ASTM standard D5470-06 [5], and the following order is listed according to the different measuring temperature. For room temperature, Madhusudana experimentally studied the effect of heat losses to the surroundings and analyzed the accuracy in TCC experiments [6]. Ding and Wang experimentally investigated the TCC of stainless steel-GFRP interface under vacuum environment [7]. Zhang et al. established a high-precision instrumentation to measure TCR using reversible heat flux mainly for electronic devices [8]. For high temperature, Liu et al. conducted experimental investigation on the TCR between high thermal conductivity C/C material and Inconel 600 up to 800 K [9]. For cryogenic temperature, Choi and Kim carried out experiment on TCR between metals below 100 K [10]. As indicated in the comprehensive review paper by Yovanovich that experiments can provide very limited and insufficient data of the TCR [11]. Meanwhile, with the fast development of computer industry and numerical methods, numerical modeling and simulating TCR becomes a more and more feasible and important approach. Numerical results of TCR simulation can provide the details of surface contacted locations which are beneficial to understand the mechanisms. Generally speaking, numerical simulation of TCR involves several aspects, including the descriptions of surface topography, the analysis of micro mechanical deformation, and the heat transfer models [1]. The contact surface topography should be described and reconstructed firstly. In this regard, the frequently-used methods can be classified into two categories: statistics of the roughness profile [12] and methods based on fractal theory [13]. The above two methods have the common characteristic that the roughness height is supposed to conform to a certain distribution function. Then the integral of the function can be adopted to figure up the number of contact spots or actual contact area. However, a number of assumptions are usually applied in these methods, leading to a great uncertainty of the results. Pennec et al. carried out the actual surface scanning work which decreased substantial uncertainty together with finite element modeling [14]. The deformation of the contact spots should be analyzed secondly. There are three deformation models: elastic, elastic-plastic and plastic. Different deformation models are mainly related to the loading pressure. Mikic [15] proposed an elastic contact model and investigated the effects of the three modes of deformation on the value of contact conductance and presented the criteria by which the deformation mode can be determined. Cooper et al. [16] proposed a plastic contact model and Yovanovich [17] proposed a further improvement of this model. Bush and Gibson adopted elastic and plastic modes of surface deformation to study the variation of thermal conductance with applied load [18].

Sridhar and Yovanovich presented an elastoplastic contact conductance model for isotropic conforming rough surfaces and compared the results with experiments [19]. The purposes of all the deformation models are to get the distribution of contact spots and the real contact area under tested contact conditions. To finally acquire the TCR values for a test condition, some specified methods and heat transfer models should be employed. Cui et al. carried out a multiscale simulation with coupling the lattice Boltzmann (LB) method and the traditional finite difference (FD) method to calculate the heat transfer between two rough surfaces in electronic packaging. The LB method and the FD method are, respectively, applied to two different regions with different meshes (fine meshes and coarse meshes) [20]. Verma and Mazumder extracted the TCC from temperature and heat flux distributions obtained from direct numerical simulations of heat conduction across the interface. No assumptions are made pertaining to the shape, size, and height of the asperities and ensuing contacts, the topography of the interface is stochastically reconstructed from commonly measured surface roughness descriptors [21]. Zou et al. developed a random number model based on fractal geometry to calculate TCC [13]. Murashov and Panin numerically simulated the contact heat transfer problem of hardened rough surfaces [22]. A basic work with surface scanning and the use of FEM for the thermal contact conduction calculation from Thompson should be acknowledged [23]. Similar conclusions are drawn about the effect of the medium in the gap in that thesis. Gou et al. proposed an approach to predict TCR based on the practical topography of the two rough surfaces using ANSYS [24]. In their study two material pairs Ti-6Al-4V—Ti-6Al-4V and C/C-SiC—high temperature ceramic (HTC) were investigated and relatively good results were obtained. From the brief review of the existing references the present authors consider that several aspects of the model and method still can be modified to improve the accuracy and efficiency. Firstly, in the previous work the radiative heat transfer influence on the TCR is neglected [22,24]. This influence is especially important for high temperature cases because TCR is positively correlated with the average temperature of the contact surfaces. Secondly, the thermal conductivity of the material used in the heat transfer model are usually based on the arithmetic mean temperature not the material regionally local temperature which could decrease the accuracy of the heat transfer model. Finally, the gap conductance is simplified by an empirical parameter TCC and an average gap distance. In fact, there are numerous contact pairs filled with gap to conduct the heat from the high temperature surface to the low temperature surface with individual gap conductance instead of an empirical parameter TCC. In order to overcome the above three inefficiencies, a more comprehensive predict model for TCR highly needs to be developed. This new model can deal with the above stated three main drawbacks.

In this paper, a new predict model is proposed to obtain the TCR of a pair of contact surfaces of Ti-6Al-4V—Ti-6Al-4V which are processed by the sand blasting and the roughness is obvious larger than the previous pair presented in reference [24]. The surface topography is acquired from the 3-D optical microscope which has a resolution in height measurement of 0.1 nm; and the measured coordinates of the roughness distribution are used to generate the numerical grid points. Then the commercial software ABAQUS is employed to implement the TCR calculation. Besides, the TCR for 12 cases under air gap with different temperatures and loading pressures are experimentally measured by a specially design test apparatus based on 1-D steady state heat flux method. The numerical results of all cases agree very well with the experimental data. In the following, the numerical model will first be presented (Section 2), focusing on how to transfer the measured surface roughness to the software ABAQUS as input data to reconstruct the rough surface. The numerical methods are fully implemented in ABAQUS generating results with temperature distribution and heat flux. And the numerical TCR can be obtained with data reduction. Then a home-made test platform will be described in Section 3. Both the numerical and test results will be presented and compared in Section 4 and several influence factors affecting on TCR are analyzed. Finally some conclusions are drawn in Section 5.

2. Numerical model

2.1. Test specimen and computational domain

Fig. 1 shows two test specimens Ti-6Al-4V and contact surfaces topography. Fig. 2 shows the schematic diagram of the two specimens and the computational domain studied. The specimen are cylinders with diameter of 48 mm and height of 52 mm. T_1 to T_6 are temperatures obtained from the thermocouples located at the drilled holes in different heights. The distance between the contact surface and the holes at the three levels are 8 mm, 16 mm, 16 mm, respectively. In each level four holes are uniformly located in the circumferential directions and each temperature is acquired from the average temperature of the four

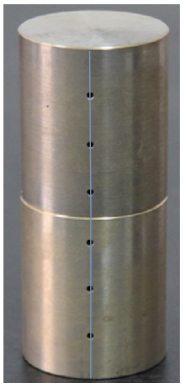

(a) Two test specimens

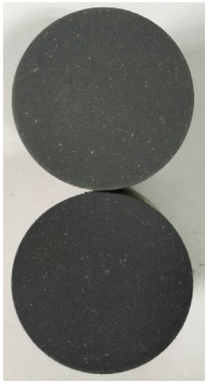

(b)Two contact surfaces

Fig. 1. Two test specimens and contact surfaces topography.

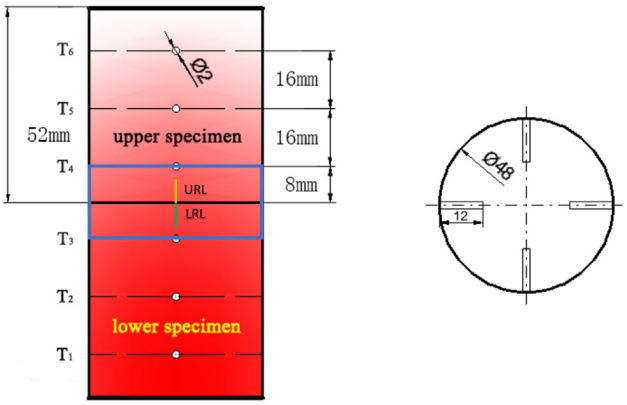

Fig. 2. Dimensions and computational domain.

thermocouples. The diameter and the depth of the holes are 2 mm and 12 mm, respectively. In order to minimize the computational cost, two models with heights of 104 mm and 16 mm are established to investigate the effect of height on the analysis results. The contact analysis results shows that deviation between the two models on the real contact area is only 0.3% when the pressure is 4.65 MPa. Hence the height of 16 mm marked by blue lines box in Fig. 2 is selected as the computational domain. In fact, four lines are equidistantly carved in sides of the each sample along the circumference as one of which demonstrated in Fig. 1(a). These four lines are used to guarantee the coincidence of the position of the samples. In order to simplify illustrating the relative contact position of the two specimens, the upper reference line (shown by URL in Fig. 2) and the lower reference line (shown by LRL) are used in the numerical model.

2.2. Rough surfaces

The 3-D surface topography of the two contact surfaces are measured with the optical microscope named Bruker Contour GT-K with vertical resolution 0.1 nm. Optical resolution includes two aspects: lateral resolution and vertical resolution. The present microscope is equipped with different magnification objectives providing a minimum lateral resolution 0.33 μm. Different vertical resolution can be achieved based on two totally different measurement technology named VSI (vertical scanning interferometry) and PSI (phase shift interferometry). The highest vertical resolution of VSI technology is 1 nm while for the PSI is 0.1 nm. The greatest advantage for the methodology of this article is the 'stitch' function by which topography of very large geometrical dimension can be measured one time. Fig. 3 shows the 3-D optical microscope measurement system. Fig. 4 shows the measured upper and

Fig. 3. Optical microscope measurement system.

lower contact surfaces topography and different colours represents different heights in different locations. The mean absolute deviation R_a and standard deviation R_q of the roughness of the lower contact surface are 21.46 μm and 31.49 μm, respectively, and for the upper contact surface are 13.36 μm and 17.95 μm, respectively. The surface topography is a multiscale description which contains microscopic roughness, mesoscopic flatness and macroscopic surface form. The flatness and surface form are both taken into account in our measurement. The z coordinate of measured data points includes these three scale values. During the experiment, the two samples were stacked on each other aligning the level with a level ruler. Hence the numerical contact model based on this practical rough topography is an accurate description of the experimental contact pair. All the measured data of surfaces topography are saved as 3-D coordinates (2-D in location and 1-D in height) shown in Fig. 5(a) and then processed with self-coded program in language Python in a pre-processing software ANSA which can provide mesh generation to ABAQUS conveniently. Coons-surfaces are selected to reconstruct the contact 3-D surfaces within every four neighbouring points and every adjacent eight measured data points are used as the nodes to generate one element.

The measured characteristic length (shown by L in Fig. 5(a)) which refers to the projection distance between two measured data points is 0.253359 mm. The measured data points in upper and lower contact surfaces have the same horizontal coordinates in 2-D location. Fig. 5 shows the process of how to reconstruct a rough surface from the measured data points. Fig. 5(a) shows the measured rough surface data points; Fig. 5(b) shows the measured data points height distribution and the whole measured size is slightly larger than the test specimen diameter 48 mm to ensure the maximum effective rough surfaces information; Fig. 5(c) shows the measured data points coons-surfaces topography reconstruction; Fig. 5(d) shows the actual computaional area coons-surfaces topography. All the labels in Fig. 5 are in millimetre unit.

The mesh independence verification is implemented firstly. The measured data points from our microscope has equal spacing in the x, y directions. We adopted two different numbers of measured data points to reconstruct the rough surface, where the number of fine meshes formed of measured data points is 4 times more than coarse meshes, as shown in Fig. 6. The detailed parameters of two different mesh numbers are shown in Table 1. The measured characteristic length of fine meshes is 0.253359 mm while that of the coarse meshes is 0.507 mm. The TCR of fine meshes is 6.7% higher than that of coarse meshes. So the fine meshes with 1,778,432 elements are selected as the final discretized mesh system. It is clear that a smaller characteristic length will present more details of the practical rough surface, however, simultaneously it will require more meshes and computational time and the increasing costs may make the simulation unable to run. On the other hand, as we

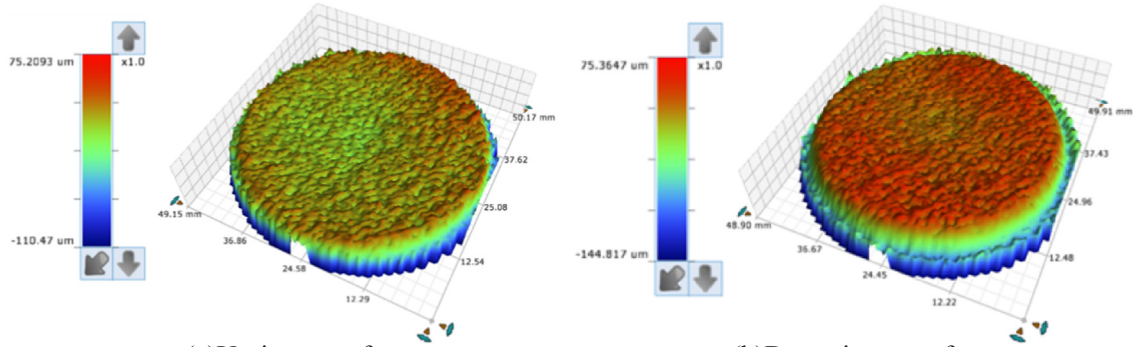

(a)Up-inner-surface (b)Down-inner-surface

Fig. 4. Measured surface topography.

all know it is impossible to create a complete model including all the surface details. In this aspect what we have done in this work is to establish a model contains as much surface details as possible within our computational ability.

Fig. 7(a) shows part of the 3-D lower contact surface topography reconstructed with the steps of Fig. 5 where 28,165 measured data points are used. These 28,165 data points formed 27,788 coons-surfaces in each contact surface. And the upper actual reconstructed rough surface can be finished with the same steps which should be presented on its opposite base. Two numerical samples are established setting the upper and lower reconstructed rough surfaces as the characteristic surfaces. Fig. 7(b) shows the simulation model meshes used in this investigation where only part of the model is demonstrated in order to observe the meshes near the contact surfaces clearly. It can be easily

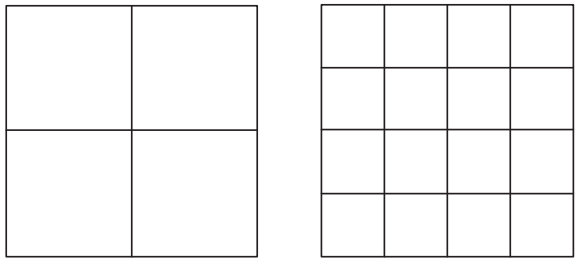

(a) Coarse meshes (b) Fine meshes

Fig. 6. Demonstration of two different meshes in mesh independence verification.

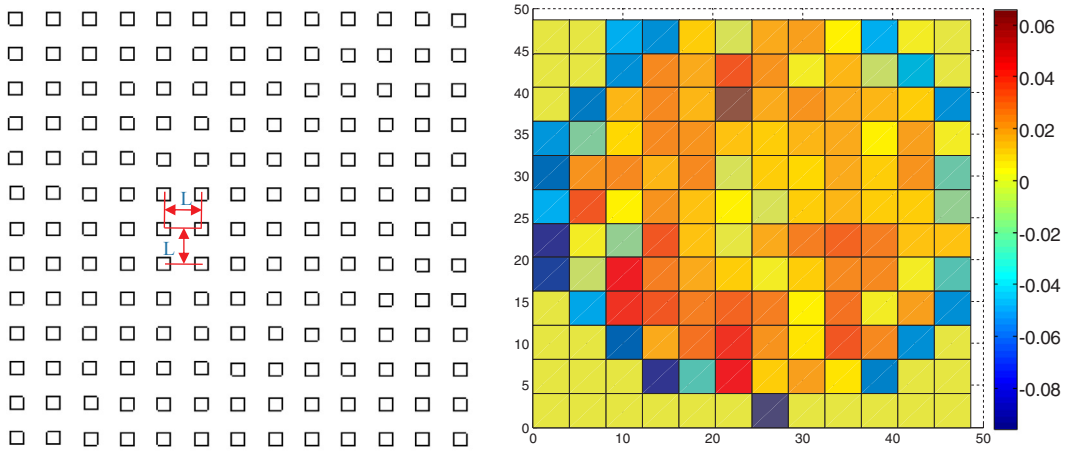

(a)Measured rough surface data points (b) Measured data points height distribution/mm

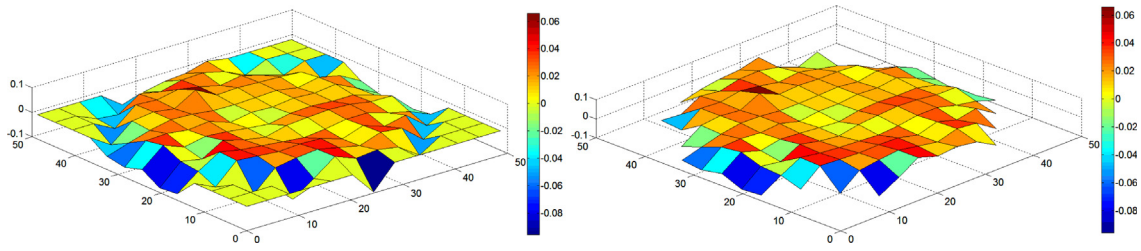

(c)Measured data points coons-surfaces topography reconstruction/mm (d)Actual computaional area coons-surfaces topography reconstruction/mm

Fig. 5. Demonstration of the process on topography reconstruction.

Table 1
Detailed parameters of two different mesh numbers.

	Numbers of measured data points	Number of elements reconstructed of contact surface	Total elements of the whole model
Coarse meshes	7,042	6,854	562,028
Fine meshes	28,165	27,788	1,778,432

seen that the meshes near the contact surfaces are denser than those far away from the contact surfaces. The whole computational model contains 1,778,432 hexahedral elements and 1,858,890 nodes. The CPU of the work station used to reconstruct rough surfaces and generate mesh are Intel(R) Xeon(R) E5-2660 v3 with frequency 2.6 GHz, and the RAM is 64 GB.

2.3. Numerical model and boundary conditions

As we discussed above, the total height of the computational region is 16 mm with the upper and lower parts 8 mm height each. The numerical model and related boundary conditions are shown in left part of Fig. 8. And the pink line in the right part of Fig. 8 clearly shows the two contact rough surfaces. Here the initial contact status of the two specimens is determined by following 'ideal' contact state. As indicated above both the upper and lower surface have one-to-one correspondent totally 27,788 coons-surfaces. Among so many cells there must be one pair of nodes which has the largest sum of the upper and lower roughness heights. This implies that when the upper and lower surfaces of this node are just in contact, all other pair of cells are not in contact. This is called ideal contact state. Once the height coordinates of the data points are obtained from the microscope, we can figure out the initial ideal contact state of the two specimens by the translational method, and the process can be seen in Fig. 9. The TCR depends on the contact surface topography and relative position of the two contact samples, rather than the absolute x, y, z coordinates of the measured data points used to reconstruct the contact rough surface. So the initial contact position is just easy for the convergence of TCR simulation, and the translational method is used to ascertain the initial contact status. In fact, there will be at least three pairs of contact points because of the upper sample's own weight leading to tiny deformation of the contact points. Here only one contact pair is assumed to simulate the initial contact status where the upper specimen's weight is transferred to the loading pressure.

As the initial ideal contact state has been created, the mechanical and heat transfer performance of the contact model is performed with ABAQUS in the light of sequential coupling method. The temperature distribution and heat flux of the whole computational model can be finally obtained from ABAQUS. And the numerical TCR can be acquired with data reduction.

The thermal contact resistance TCR is defined by Eq. (1):

$$\mathrm{TCR} = \frac{\Delta T}{q} = \frac{T_{down} - T_{up}}{q} \tag{1}$$

where T_{down} and T_{up} are the average temperature of the down-inner-surface and up-inner-surface shown in Fig. 10, respectively. These two contact surfaces average temperatures are calculated from the arithmetic average temperature of all the nodes on the contact surfaces. ΔT is the temperature difference between T_{down} and T_{up}. q is the average heat flux of the axial direction flows through the contact surfaces. The boundary conditions for the mechanical and heat transfer calculation are defined as follows:

$$\begin{aligned}
&U_1 = U_2 = 0;\\
&\text{Up-surface: } P = P_0;\\
&T = T_4\\
\\
&U_1 = U_2 = 0;\\
&\text{Up-round: } UR_1 = UR_2 = UR_3 = 0;\\
&q = 0\\
\\
&U_1 = U_2 = U_3 = 0;\\
&\text{Down-surface: } UR_1 = UR_2 = UR_3 = 0;\\
&T = T_3\\
\\
&U_1 = U_2 = 0;\\
&\text{Down-round: } UR_1 = UR_2 = UR_3 = 0;\\
&q = 0
\end{aligned} \tag{2}$$

where U_1, U_2, U_3 represent displacement in x, y, z directions respectively. UR_1, UR_2, and UR_3 represent rotation displacement in three spatial angles respectively. P represents the pressure in z directions. P_0 represents the pressure measured by the pressure sensor. T represents the temperature, T_3 and T_4 represent the temperatures obtained from the thermocouples located in two cross sections shown in Fig. 10. In addition, the temperature distribution of the top surface in the model for vacuum has a maximum difference of 1.1 °C which is in the uncertainty range of the thermocouple. Therefore T_3 and T_4 can be implemented as the boundary condition of the up and down surfaces. Twelve cases under three different loading pressures and four different heating temperatures are experimentally studied and the detailed test condition information are listed in Table 2. The 'up-inner-surface' in Fig. 8 refers

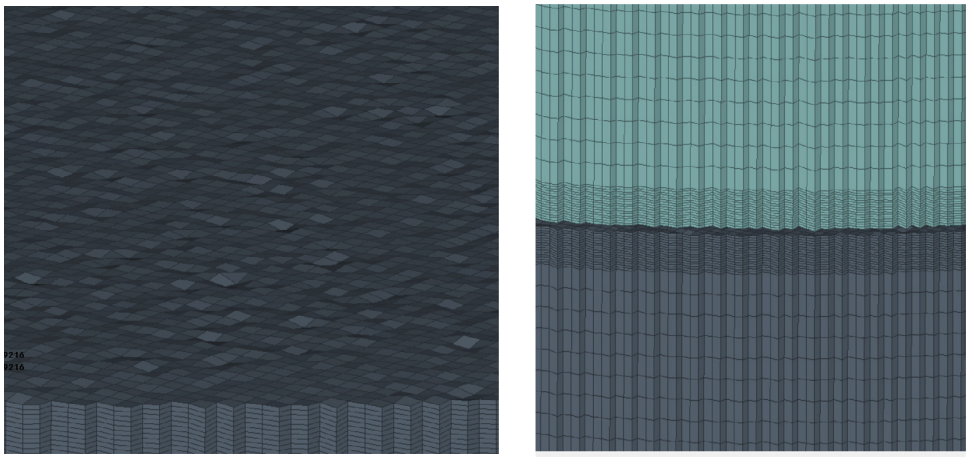

(a) Part of the reconstructed contact surface(top view) (b) Part of the model meshes(side view)

Fig. 7. Part of the reconstructed contact surface and meshes.

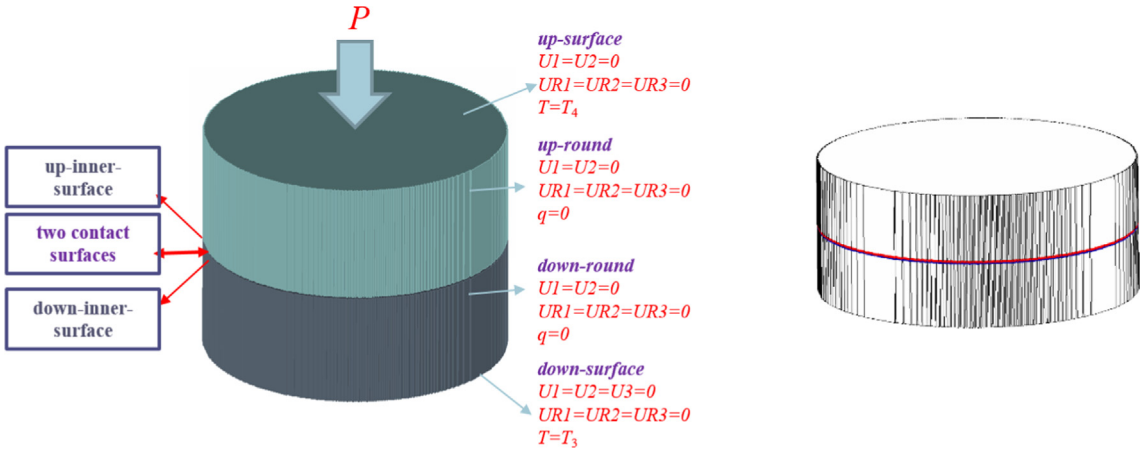

Fig. 8. Numerical model and boundary conditions.

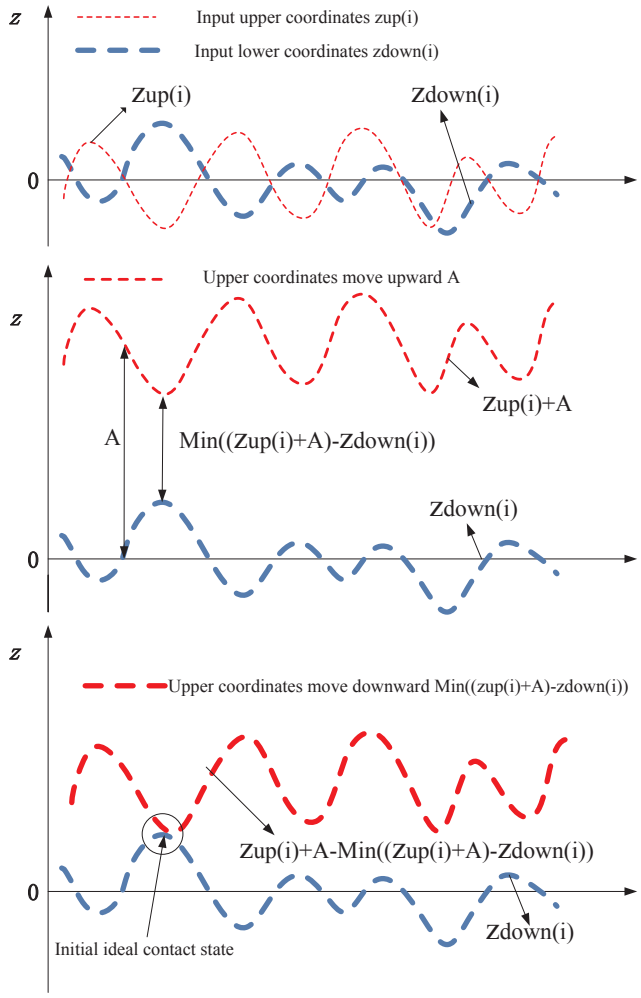

Fig. 9. Process of creating the initial ideal contact state.

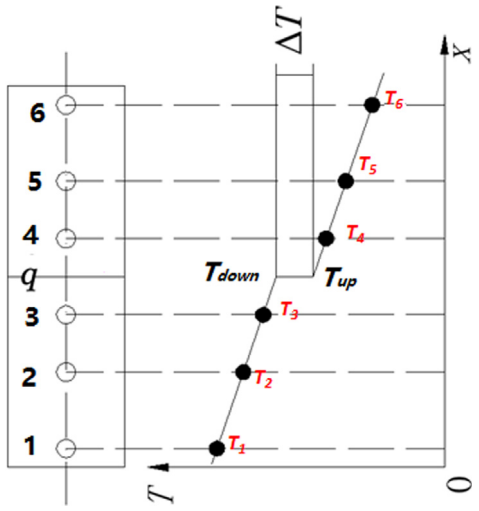

Fig. 10. Temperature drop and heat flux through the contact surfaces.

Table 2
The experimental measured temperatures and loading pressure.

Loading pressure (MPa)	Case numbers	Heating temperature (°C)	T_3 (°C)	T_4 (°C)	T_1 (°C)	T_6 (°C)
4.65	A	400	243.9	183.8	324.9	91.1
	B	500	307.2	231.8	406.0	113.1
	C	600	373.0	282.1	488.1	137.5
	D	700	435.9	331.5	566.8	161.5
7.78	A	400	247.4	188.9	330.5	92.8
	B	500	310.1	235.9	411.7	113.2
	C	600	374.4	285.0	492.3	136.1
	D	700	436.7	334.5	570.8	159.4
12.08	A	400	247.2	189.7	331.8	92.1
	B	500	311.0	237.9	413.7	113.0
	C	600	372.5	285.0	492.7	133.3
	D	700	435.8	336.2	572.7	154.3

to the upper surface of the contact surfaces pair while the 'down-inner-surface' in Fig. 8 refers to the lower surface of the contact surfaces pair.

2.4. Meshes and numerical method

In this study the C3D8 linear element is used to solve the mechanical problem, where C in C3D8 indicates this is a continuum element, 3D indicates three-dimensional. DC3D8 is the corresponding thermal model element to solve the diffusive (which is the implication of the first letter 'D') heat transfer problem. And '8' implies that each element is an eight-node linear rick, as shown in Fig. 11.

The full Newton method is selected as the solution technique for solving the nonlinear equations and load is numerically varied with a ramp linearly step by step. The Lagrangian point of view is used for modeling the mechanical capabilities in ABAQUS because the material properties are history-dependent and the Lagrangian perspective makes the simulation easy. Isoparametric interpolation is defined in terms of

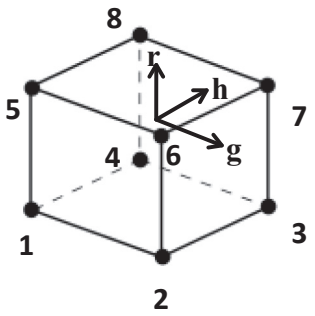

Fig. 11. Linear element (8-node brick, C3D8).

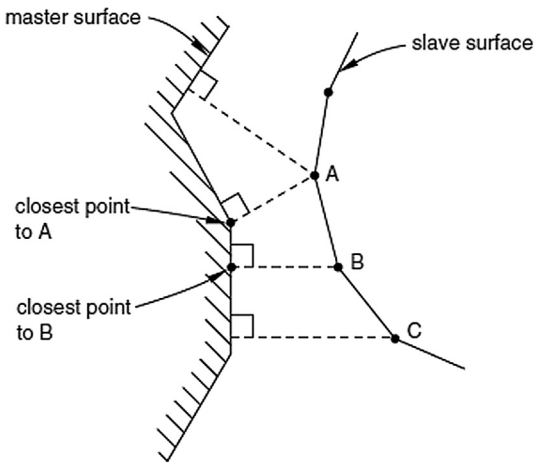

Fig. 12. Node-to-surface contact discretization [26].

the isoparametric element coordinates *g*, *h*, *r* shown in Fig. 11. They each span the range −1 to +1 in an element. The node numbering convention used in ABAQUS for isoparametric elements is also shown in Fig. 11. The interpolation function can be expressed as Eq. (3), where u represents the node displacement. Full Gauss integration is used to integrate the element's internal forces and stiffness.

There are three essential aspects to deal with the contact problem with ABAQUS: assignment of "master" and "slave" roles to the contact surfaces, a contact discretization, and a tracking approach [26]. In this study, down-inner-surface is processed as the master surface while up-inner-surface is processed as the slave surface. The contact direction is based on the normal of the master surface. Node-to-surface

$$u = \tfrac{1}{8}(1-g)(1-h)(1-r)u_1 + \tfrac{1}{8}(1+g)(1-h)(1-r)u_2 + \tfrac{1}{8}(1+g)(1+h)(1-r)u_3 + \tfrac{1}{8}(1-g)(1+h)(1-r)u_4 + \tfrac{1}{8}(1-g)(1-h)(1+r)u_5 + \tfrac{1}{8}(1+g)(1-h)(1+r)u_6 + \tfrac{1}{8}(1+g)(1+h)(1+r)u_7 + \tfrac{1}{8}(1-g)(1+h)(1+r)u_8 \quad (3)$$

Table 3
Ti-6Al-4V properties at different temperatures.

T/(°C)	Young's Modulus/ (GPa)	Poisson's ratio	Yield strength/ (MPa)	Plastic strain	Thermal conductivity/ (W/m·K)
RT	120.59	0.286			6.8
100	120.05	0.284			7.4
200	115.5	0.294	860	0	8.7
300	113.39	0.299	980.6	0.1	9.8
400	108.1	0.314			10.3
500	92.98	0.352			11.8

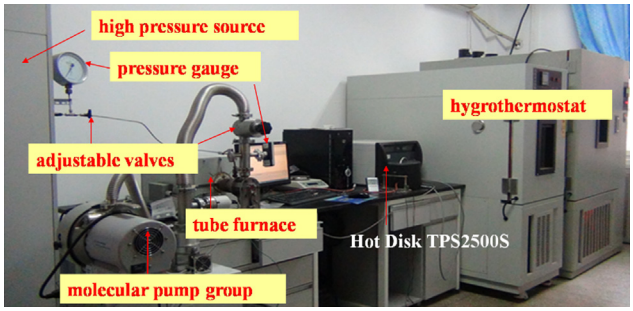

Fig. 14. Thermal conductivity measurement platform.

contact discretization is adopted as the contact discretization and finite sliding is selected as the tracking approach to account for the relative motion of two interacting surfaces in mechanical contact simulations. Now brief introductions of contact discretization and tracking approach are cited from ABAQUS [26].

With traditional node-to-surface discretization the contact conditions are established such that each"slave" node on one side of a contact interface effectively interacts with a point of projection on the"master" surface on the opposite side of the contact interface (see Fig. 12). Thus, each contact condition involves a single slave node and a group of nearby master nodes from which values are interpolated to the projection point. The slave nodes are constrained not to penetrate into the master surface; however, the nodes of the master surface can, in principle, penetrate into the slave surface. Fig. 13 shows the comparison of contact enforcement for different master-slave assignments [26].

Tracking approach in ABAQUS implies the accounting for the relative motion of two interacting surfaces in mechanical contact simulations. Finite-sliding contact is the most general tracking approach and allows for arbitrary relative separation, sliding, and rotation of the contacting surfaces. For finite-sliding contact the connectivity of the currently active contact constraints changes upon relative tangential motion of the contacting surfaces [26].

All the convergence criterions for force and heat flux are in the default settings of the software. Criterion for displacement correction is 1.000E−02 and for residual force is 5.000E−03. Criterion for temperature correction is 1.000E−02 and for residual heat flux is

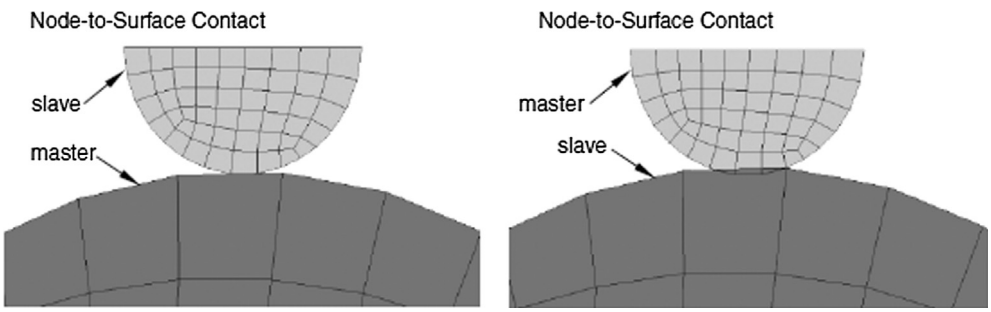

Fig. 13. Comparison of contact enforcement for different master-slave assignments [26].

Table 4
Air properties at different temperature under atmosphere condition.

Temperature (°C)	100	120	140	160	180	200	250	300	350	400
Thermal conductivity × 10^2 (W/m·K)	3.21	3.34	3.49	3.64	3.78	3.93	4.27	4.60	4.91	5.21

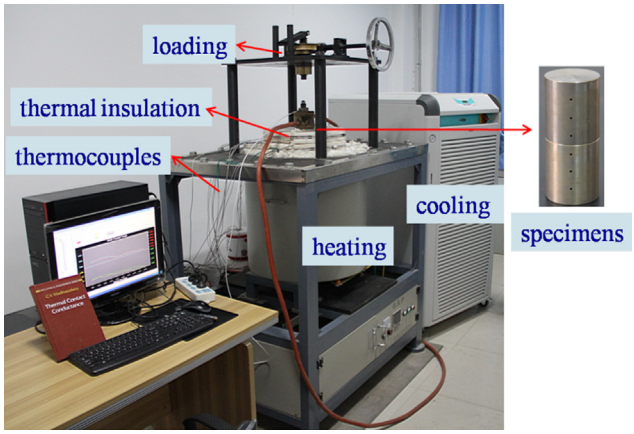

Fig. 15. Thermal contact resistance measurement platform.

5.000E − 03.

2.5. Material properties

Table 3 lists the mechanical and thermal properties of Ti-6Al-4V adopted in the numerical simulation. In the table, the Young's modulus, Poisson's ratio and thermal conductivity are regarded as the temperature-dependent and typical values at six temperatures are provided.

Here the thermal contact resistance under loading pressure of 4.65 MPa and heating temperature of 400 °C is taken as an example to compare the results from purely elastic model and elastic-plastic model. The thermal contact resistance from elastic-plastic model is 8.30×10^{-4} K·m^2/W while the result from purely elastic is 8.29×10^{-4} K·m^2/W with a deviation less than 0.13%. So in this study the constitutive equation of the plastic problem is described by the equivalent plastic modulus and the yield limit. When the stress is greater than the yield limit, assuming that the material stress and strain are still linearly related and the slope is 1/100 of the elastic modulus.

The yield stress and plastic strain are assigned as 860 MPa, 0 and 980.6 MPa, 0.1, respectively. The thermal conductivity typical values at six temperatures are measured with our Hot Disk TPS2500S, the measurement platform is shown in Fig. 14. The air properties at different temperature under atmosphere condition are displayed in Table 4.

2.6. Gap heat transfer

The convective heat transfer and the relative equivalent thermal conductivity becomes negligible in the materials composed of pore sizeless than 1 mm at ambient pressure [25]. In this study, the size of the irregularities is at the order of micrometer so the convective heat transfer can be neglected. The conductive and radiative heat transfer between the gap is considered and simulated. Heat conduction across the interface is defined by [26]:

$$q_c = k(\theta_A - \theta_B) \tag{4}$$

where q_c is the conductive heat flux per unit area crossing the interface from point A on one surface to point B on the other, θ_A and θ_B are the temperatures of the points on the surfaces, and k is the gap conductance. Point A is a node on the slave surface, and point B is the location on the master surface contacting the slave node or, if the surfaces are not in contact, the location on the master surface with a surface normal that intersects the slave node. The gap conductance is determined by

$$k = k(d, \bar{\theta}) = \frac{\lambda(\bar{\theta})}{d} \tag{5}$$

where d is the clearance between A and B, $\bar{\theta} = \frac{1}{2}(\theta_A + \theta_B)$ is the average of the surface temperatures at A and B; $\lambda(\bar{\theta})$ is the air conductivity at temperature of $\bar{\theta}$. Furthermore, this method can be used to deal with other gap medium other than air which can fully fill in the gap. The radiative heat transfer can be determined by the model of two parallel plates where the upper surface of the contact materials is assumed to be parallel to the lower surface. Then, the radiative heat flux between the two surfaces can be expressed as [26,27]:

$$q_r = C[(\theta_A - \theta_Z)^4 - (\theta_B - \theta_Z)^4] \tag{6}$$

$$C = \frac{F\sigma}{\frac{1}{\varepsilon_A} + \frac{1}{\varepsilon_B} - 1} \tag{7}$$

where q_r is the radiative heat flux crossing the gap at this point; θ_A and θ_B are the temperatures of the two surfaces in °C; θ_Z is the value of absolute zero temperature on the temperature scale being used, $\theta_Z = -273K$; σ is the Stefan-Boltzmann constant, ε_A and ε_B are the emissivity of the upper and lower surface, respectively, and F is the effective view factor, which corresponds to how much part of the

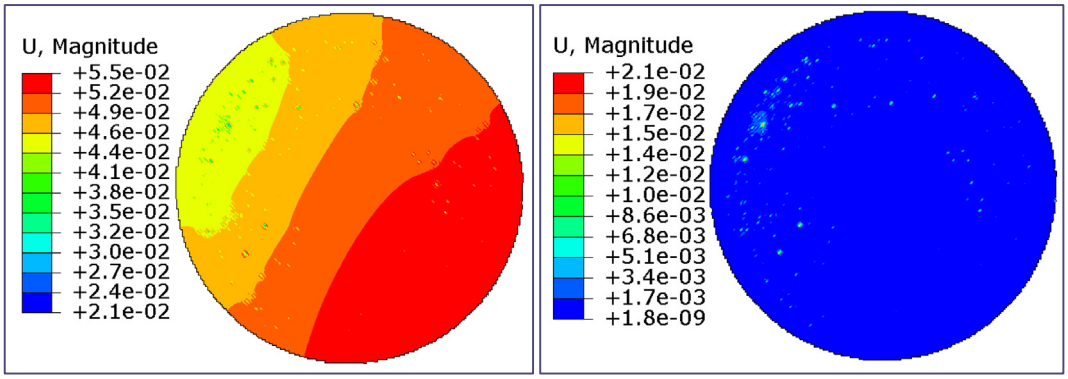

(a) up_inner_surface (b) down_inner_surface

Fig. 16. Displacement distribution of two contact surfaces (P = 4.65 MPa).

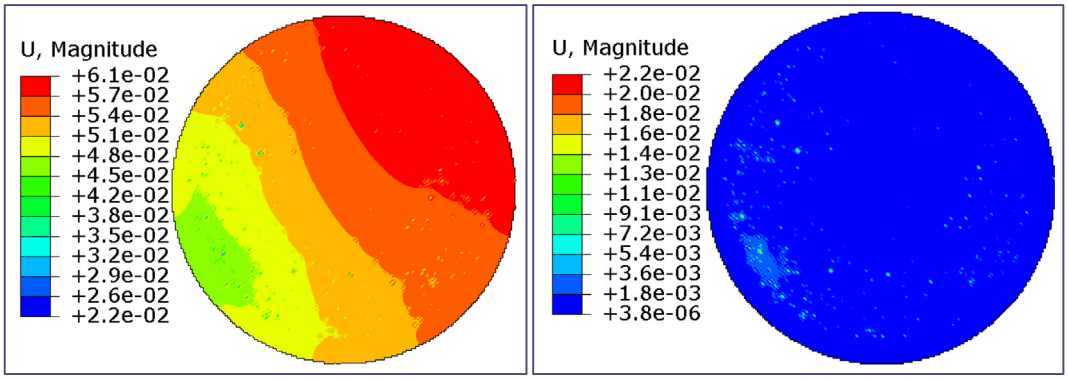

Fig. 17. Displacement distribution of two contact surfaces (P = 7.78 MPa).

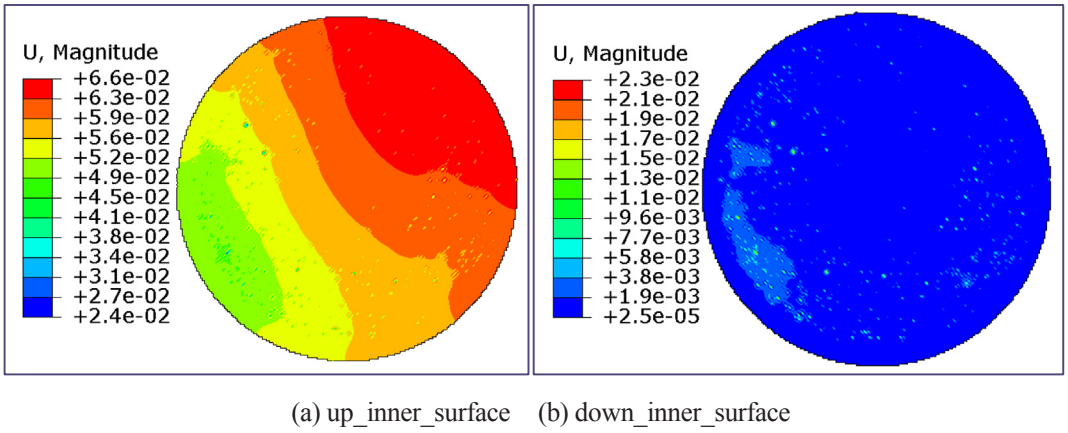

Fig. 18. Displacement distribution of two contact surfaces (P = 12.08 MPa).

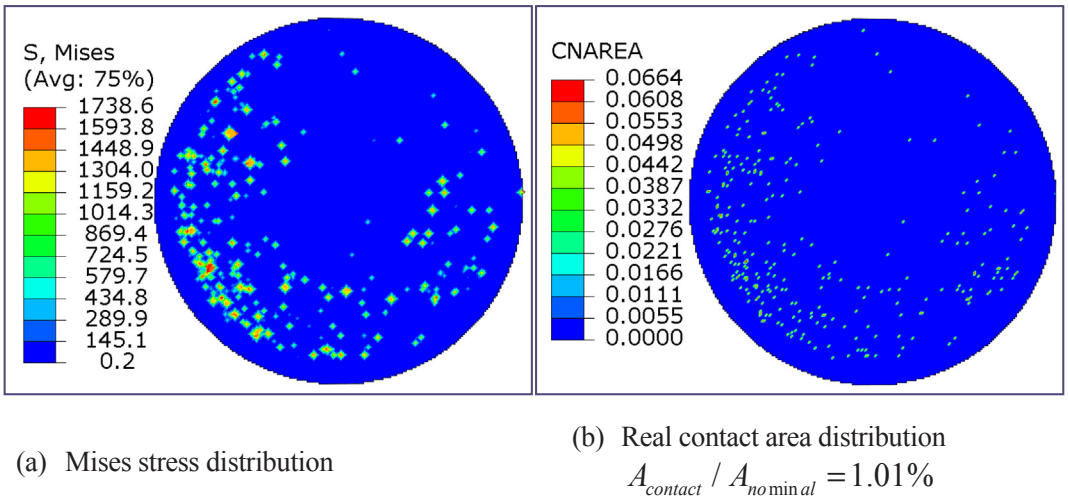

Fig. 19. Mises stress and real contact area distribution of up-inner-surface (P = 4.65 MPa).

master surface can be viewed from the slave surface. In fact, the view factor F is defined as a function of the clearance d, and should have a value between 0.0 and 1.0. Here the value of F is assumed to be 1 since the characteristic length (0.253359 mm) is much larger than the clearance d in each contact pair.

3. Experimental platform

The experimental platform shown in Fig. 15 is established based on the 1-D steady state heat conduction principle. It mainly includes six parts: (1) heating part; (2) cooling part; (3) thermal insulation part; (4) temperature measuring part (thermocouples); (5) loading part; (6) specimens. As indicated above, the temperature differences at the contacting interfaces are achieved by the heating and cooling part, as shown in Fig. 2 where T_1 to T_6 are obtained from the thermocouples. The thermal insulation part is employed to guarantee the approximately ideal 1-D steady state heat conduction. The different pressures are originated from the worm and gear loading part. The average

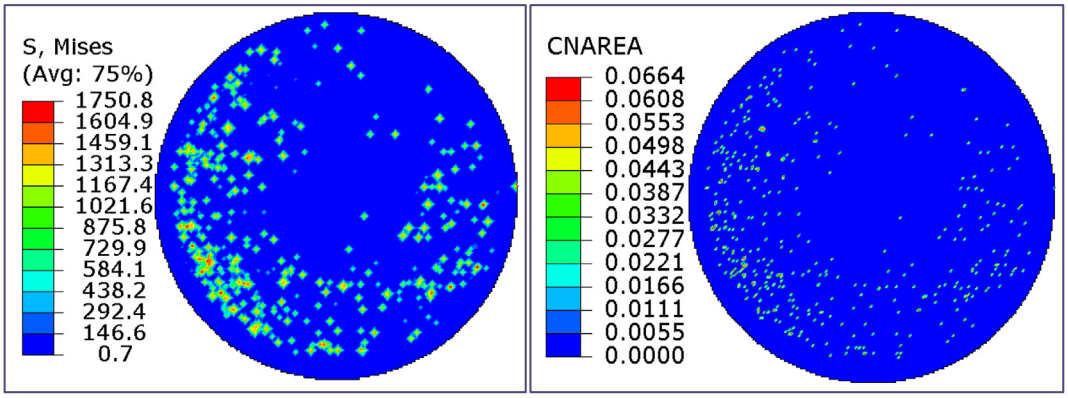

Fig. 20. Mises stress and real contact area distribution of up-inner-surface (P = 7.78 MPa).

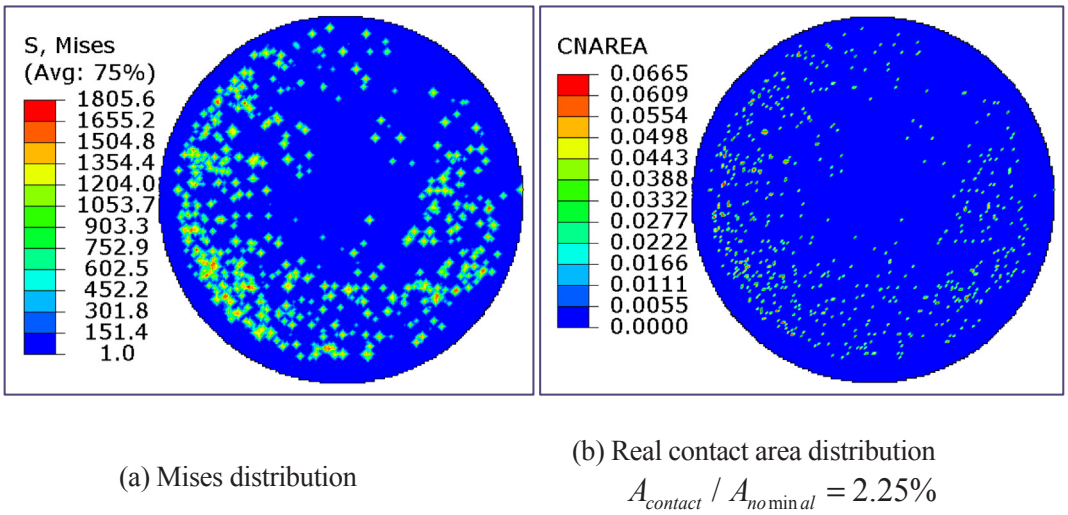

Fig. 21. Mises stress and real contact area distribution of up-inner-surface (P = 12.08Mpa).

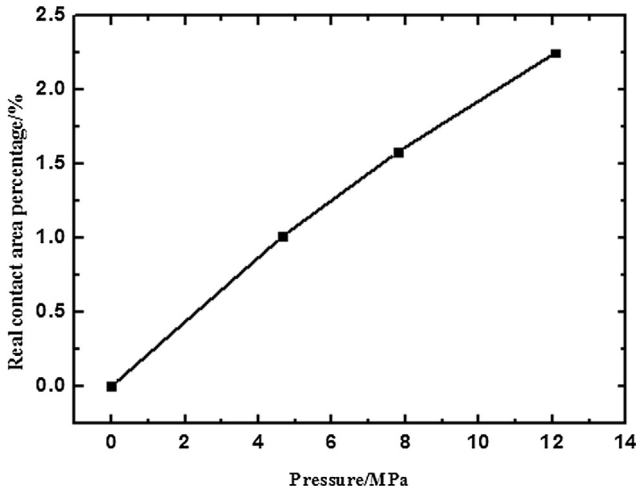

Fig. 22. Real contact area percentage vs. loading pressure.

temperature of two contact surfaces T_{down} and T_{up} are determined by outwards interpolation with measured temperatures T_1 to T_6, and the heat flux q is arithmetic average of the flux flowing through locations 2–3 and 4–5 in Fig. 2. Then the TCR is calculated by Eq. (1) with temperature difference $T_{down}-T_{up}$ and heat flux q. The TCR of 12 cases with four different temperatures and three loading pressures of air gap are experimentally measured to verify the numerical results with the same boundary conditions. The measurement cases under three different loading pressures and four different heating temperatures are listed in Table 2 with the corresponding temperatures T_3 and T_4.

4. Results and discussion

The static analysis for displacement and stress will be presented first, followed by the steady state heat transfer analysis. Then the results of the predicted thermal contact resistances will be provided and compared with the test data. The influence of interstitial medium thermal conductivity, radiation effect and solid thermal conductivity on TCR are analyzed.

4.1. Static analysis

4.1.1. Displacement distribution

Figs. 16–18 show the U magnitude (displacement vector norm of three directions) of the two contact surfaces named up-inner-surface and down-inner-surface under loading pressures at 4.65 MPa, 7.78 MPa,

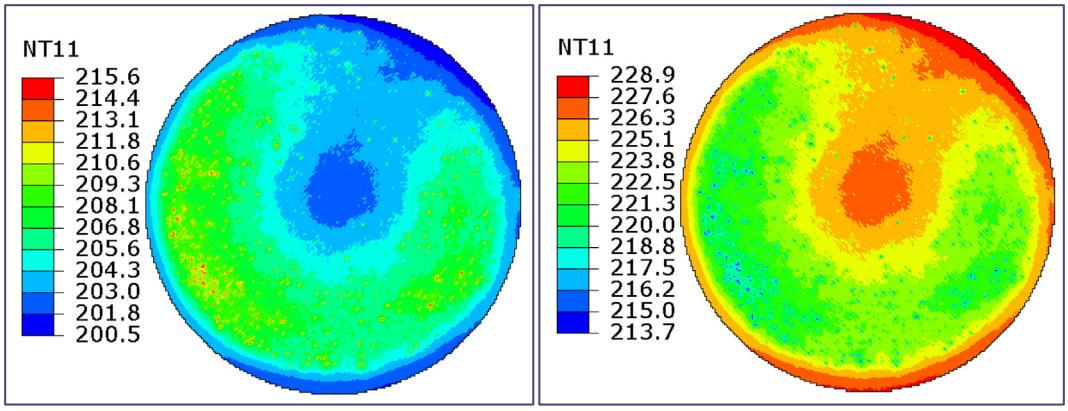

(a1) T_{up} =205.3℃ (a2) T_{down} =224.1℃

(a) P=4.65MPa, ΔT =18.8℃

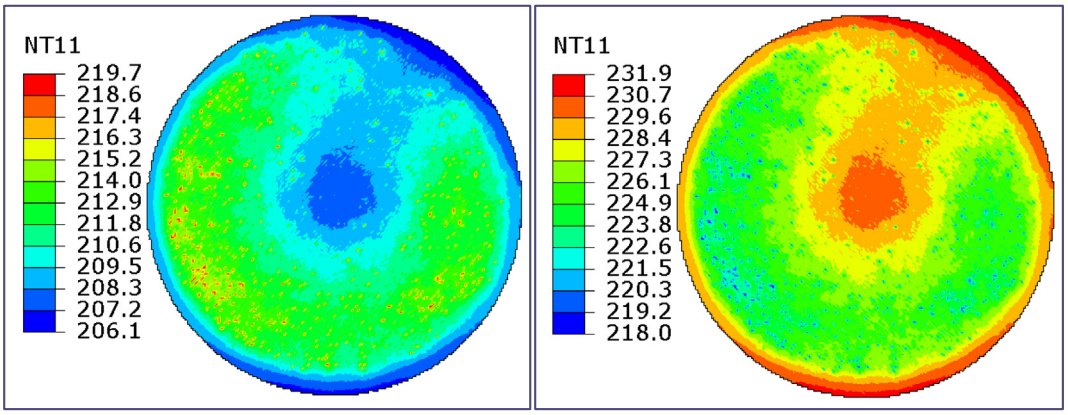

(b1) T_{up} =210.8℃ (b2) T_{down} =227.1℃

(b) P=7.78MPa, ΔT =16.3℃

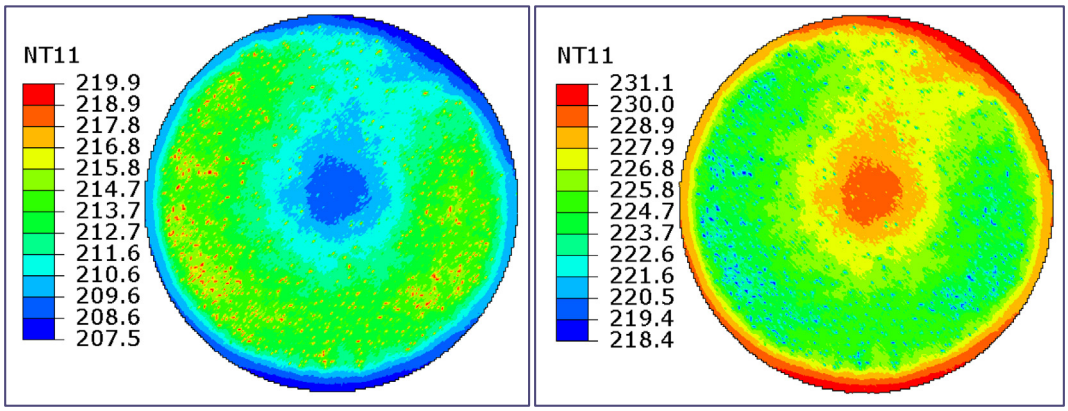

(c1) T_{up} =212.2℃ (c2) T_{down} =226.3℃

(c) P=12.08MPa, ΔT =14.1℃

Fig. 23. Temperature distribution of two contact surfaces (heating temperature 400 ℃).

12.08 MPa, respectively. All the labels are in millimetre unit. From Figs. 16–18 following results can be obtained: First of all, U magnitude of up-inner-surface is several orders higher than that of down-inner-surface because the bottom surface is fixed with encastre. Secondly, U magnitude distribution is non uniform in both up-inner-surface and down-inner-surface. Thirdly, U magnitude in up-inner-surface is at the order of 10^{-2} mm under the three loading pressures while the minimum U magnitude in down-inner-surface is at the order of 10^{-9} mm, 10^{-6} mm, 10^{-5} mm, respectively. Finally, U magnitude increase with the loading pressure in both contact surfaces.

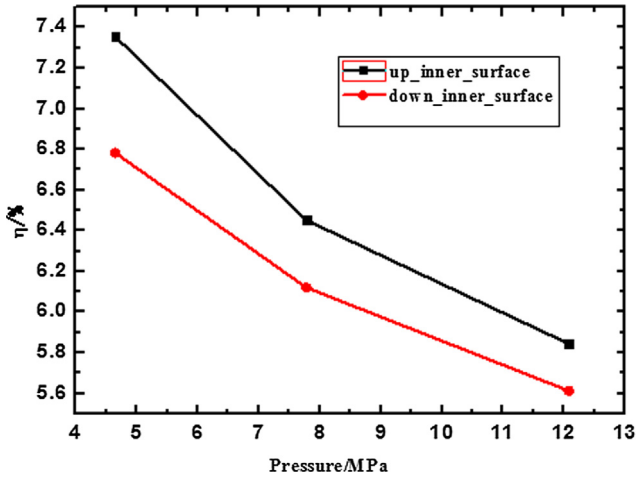

Fig. 24. Temperature nonuniformity coefficient vs. loading pressure (heating temperature 400 °C).

4.1.2. Contact area and stress distribution

Figs. 19–21 show the Mises stress and real contact area distribution of up-inner-surface under loading pressures of 4.65 MPa, 7.78 MPa, 12.08 MPa, respectively. The Mises stress is in MPa unit and real contact area is in mm^2 unit. Here the Mises stress is often used in determining whether an isotropic and ductile metal will yield when subjected to a complex loading condition. This is accomplished by calculating the Mises stress and comparing it to the material's yield stress, which constitutes the Mises yield criterion. The colorful spots are the real contact and stress concentration areas. And the proportions of the real contact area over nominal area is only about 1.01%, 1.58%, 2.25%, respectively. The maximum Mises stress increases with the loading pressure, and the corresponding values under these three loading pressures are 1739 MPa, 1751 MPa and 1806 MPa, respectively. Fig. 22 shows the real contact area percentage vs. loading pressure and a conclusion can been drawn that the real contact area increases with the loading pressure in the range of present study. Bowden and Tabor had a conclusion that the actual area of contact for most metallic surfaces is only about 1–2% of the nominal contact area even at relatively high contact pressures of the order of 10 MPa [27]. Our numerical simulation results agree well with their conclusion. The main purpose of the static analysis is to obtain the displacement of the nodes, then the stress and stain can be acquired easily. After the deformation is determined, the new position of the nodes and elements is obtained to make the steady state heat transfer analysis.

4.2. Heat transfer analysis

Temperature difference is defined as

$$\Delta T = T_{down} - T_{up} \tag{8}$$

Temperature nonuniformity coefficient is defined as

$$\eta = \frac{T_{max} - T_{min}}{\overline{T}} \tag{9}$$

where T_{max} and T_{min} are the maximum and minimum temperatures of the down-inner-surface or up-inner-surface, respectively. $\overline{T}$ is the average temperature of the down-inner-surface or up-inner-surface.

The temperature distribution is studied under four different heating temperatures and three different loading pressures. For the simplicity of presentation, Fig. 23 only shows the temperature distribution of two contact surfaces at heating temperature 400 °C under loading pressures at 4.65 MPa, 7.78 MPa, 12.08 MPa, respectively. The left sides of Fig. 23 show the temperature distribution of up-inner-surface and the right sides show the temperature distribution of down-inner-surface. The temperature difference decreases with the loading pressure from 18.8 °C to 14.1 °C. Fig. 24 shows the temperature nonuniformity coefficient vs. loading pressure of two contact surfaces at heating temperature 400 °C. The temperature nonuniformity coefficient similarly decreases with the loading pressure.

4.3. Predicted thermal contact resistance and comparison with the experimental results

The deviation between numerical and experimental is defined as

$$\text{Deviation} = \frac{TCR_{Exp.} - TCR_{Num.}}{TCR_{Exp.}} \tag{10}$$

The comparison of the experimental and numerical results are listed in Tables 5–7 under different test conditions presented in Table 2. The numerical results of air gap with radiation condition is adopted for comparison because the simulation conditions of this model are most agreeable with the measurement. The average temperature of up-inner-surface and down-inner-surface are listed in Tables 5–7. Besides, the temperature difference and the average heat flux between the two contact surfaces are also showed in order to give detailed comparisons between the experimental and numerical results. The temperature differences and the average heat fluxes both increase with the heating temperature while the TCR decreases with the heating temperature. It can be seen that the numerical results agree very well with the experimental results with the largest deviation 9.57% in Case A under loading pressure 7.78 MPa. Only the three deviations of Case A are higher than 5% while for all other 9 cases (75% of the total) their deviations are within 5%. The maximum deviations between the numerical data and experimental results only occur to Case A, since Case A is under the lowest heating temperature of 400 °C which will lead to the lowest temperature distribution in the test samples. The temperature measurement error is the biggest when the accuracy of thermocouples is a constant. To the authors' knowledge the agreement between measured and simulated results is comparatively high. Hence the new model proposed can deal with the three main drawbacks of traditional TCR theoretical models.

4.4. Influence factors analysis

4.4.1. Interstitial medium

Three different kinds of interstitial mediums are numerically simulated, e.g., vacuum, air and conductive silicone grease. The air thermal conductivities at different temperature are listed in Table 4 and the thermal conductivity of the grease is supposed to be 2 W/m·K at all

Table 5
Experimental and numerical TCR results under loading pressure 4.65 MPa.

Cases	Experimental results					Numerical results					Deviation (%)
	T_{up} (°C)	T_{down} (°C)	ΔT (°C)	q (W/m^2)	TCR × 10^4 (K·m^2/W)	T_{up} (°C)	T_{down} (°C)	ΔT (°C)	q (W/m^2)	TCR × 10^4 (K·m^2/W)	
A	206.2	223.9	17.7	22,850	7.75	205.3	224.1	18.8	22,697	8.30	7.11
B	260.3	282.5	22.2	30,422	7.30	259	282.2	23.2	30,631	7.57	3.80
C	316.6	344.1	27.5	38,470	7.15	314.6	341.9	27.3	38,960	7.01	−1.97
D	371.8	402.9	31.1	46,909	6.63	369.4	400.4	31	46,892	6.61	−0.28

Table 6
Experimental and numerical TCR results under loading pressure 7.78 MPa.

Cases	Experimental results					Numerical results					Deviation (%)
	T_{up} (°C)	T_{down} (°C)	ΔT (°C)	q (W/m^2)	TCR × 10^4 (K·m^2/W)	T_{up} (°C)	T_{down} (°C)	ΔT (°C)	q (W/m^2)	TCR × 10^4 (K·m^2/W)	
A	212.1	227.1	15.0	23,545	6.37	210.8	227.1	16.3	23,350	6.98	9.57
B	265.4	285	19.6	31,370	6.25	263.9	284.2	20.3	31,703	6.42	2.73
C	320.6	345	24.4	39,493	6.18	318.4	342.4	24	40,169	5.97	3.29
D	376.1	403.1	27.0	48,178	5.60	373.3	400.2	26.9	48,120	5.59	−0.25

Table 7
Experimental and numerical TCR results under loading pressure 12.08 MPa.

Cases	Experimental results					Numerical results					Deviation (%)
	T_{up} (°C)	T_{down} (°C)	ΔT (°C)	q (W/m^2)	TCR × 10^4 (K·m^2/W)	T_{up} (°C)	T_{down} (°C)	ΔT (°C)	q (W/m^2)	TCR × 10^4 (K·m^2/W)	
A	213.3	226.6	13.3	23,934	5.56	212.2	226.4	14.2	23,980	5.88	5.81
B	267.9	285.6	17.7	31,871	5.55	266.5	284.2	17.7	32,678	5.42	−2.47
C	321.2	342.5	21.3	40,183	5.30	319.3	339.9	20.6	40,825	5.05	−4.81
D	378.6	401.6	23.0	49,090	4.69	376.6	399.4	22.8	48,161	4.73	1.04

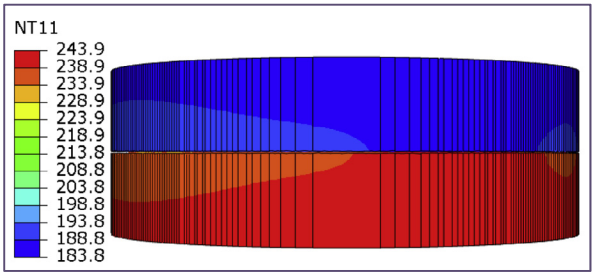

(a) Vacuum

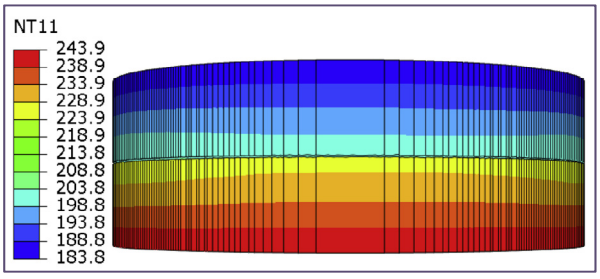

(b) Air

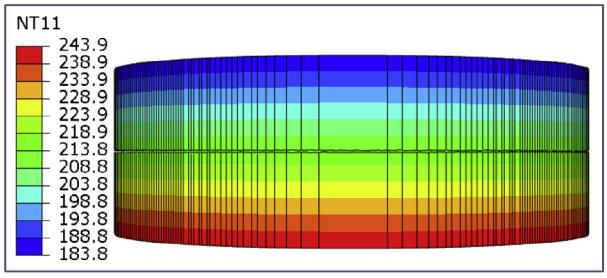

(c) Conductive silicone grease

Fig. 25. Whole model temperature distribution of three different interstitial mediums (P = 4.65 MPa, Heating temperature 400 °C).

the temperature studied. The heat transfer analysis of the whole model is investigated under three different kinds of interstitial mediums at all the 12 cases listed in Table 2. Here we take the loading pressure at 4.65 MPa and heating temperature at 400 °C as an example to analyze the differences. Fig. 25 shows the whole model temperature distribution of three different interstitial mediums. As can be seen that the model in conductive silicone grease condition has the most uniform temperature distribution while in vacuum condition has the most nonuniform temperature distribution. The same situation can be observed in Fig. 26 which displays the temperature distribution of up-inner-surface and down-inner-surface with three different interstitial mediums. The temperature ranges of up-inner-surface with vacuum, air and conductive gap are 180.7–216.7 °C, 200.5–215.6 °C and 213.0–215.1 °C, respectively. And the average temperature are 187.1 °C, 205.3 °C and 214.6 °C, respectively. The temperature ranges of down-inner-surface with vacuum, air and conductive gap are 211.8–246.8 °C, 213.7–228.9 °C and 214.8–217.0 °C, respectively. And the average temperature are 240.9 °C, 224.1 °C and 215.3 °C, respectively. It can be seen that the temperature range of conductive silicone grease is the smallest while of the vacuum gap is the largest, and the air gap is in between. The larger gap conductivity increases the conduction heat transfer between two contact surfaces leadings to the more uniform temperature distribution. Fig. 27 shows heat flux distribution of up-inner-surface of three different interstitial mediums. The heat flux in real contact area is obviously larger than that in non-contact area in air gap due to the thermal conductivity of air is much smaller than the solid, and there is no heat flux when the gap is in vacuum. This gives a good explanation of heat flux lines are constrained to actual contact spots when TCR produces. But when the gap is filled with conductive silicone grease whose thermal conductivity (2 W·m^{-1}·K^{-1}) is close to the solid thermal conductivity (about 10 W·m^{-1}·K^{-1}), the heat flux lines is comparative uniform flowing through the contact surfaces seen in Fig. 27(d). The unit in Fig. 27 is kW/m^2. The results of TCR at three different kinds of mediums are demonstrated in Fig. 28. From the figure we can see that the interstitial gap medium thermal conductivity has a significant effect on the TCR. The TCR decreases with the increase in interstitial gap thermal conductivity. The TCR of vacuum gap is 10 times larger than that of air gap while the TCR of air gap is 50 times larger than that of grease gap under the same boundary conditions.

In order to reveal the importance of air gap heat conduction, Table 8 shows the numerical results of air and vacuum gap with radiation under the loading pressure 7.78 MPa and at heating temperature 600 °C. The heat transfer between two contact surfaces with the air gap consists of three parts: (a) conduction through the actual contact spots of two solids; (b) conduction through the air; (c) radiation heat transfer between the two surfaces of gaps. While the heat transfer between two contact surfaces with the vacuum gap consists of two parts: (a) and (c). The results in Table 8 show that the average heat flux through the contacted

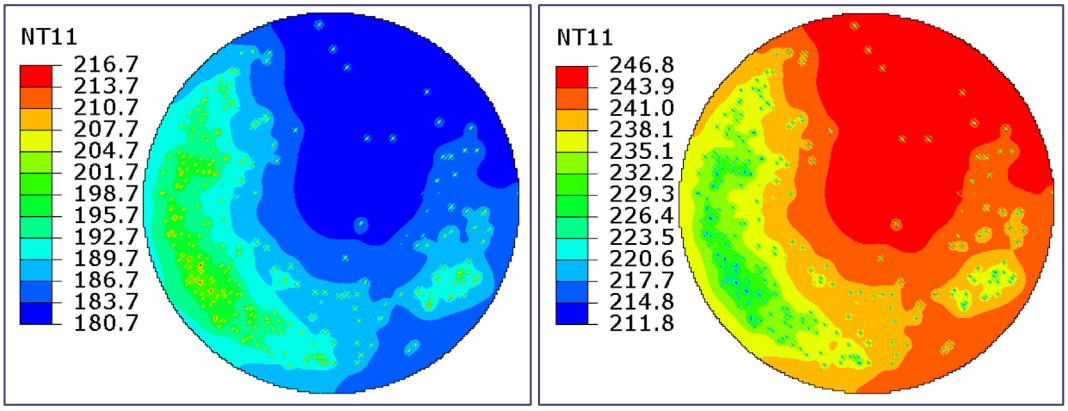

(a1) T_{up}=187.1 ℃ (a2) T_{down}=240.9 ℃

(a)Vacuum

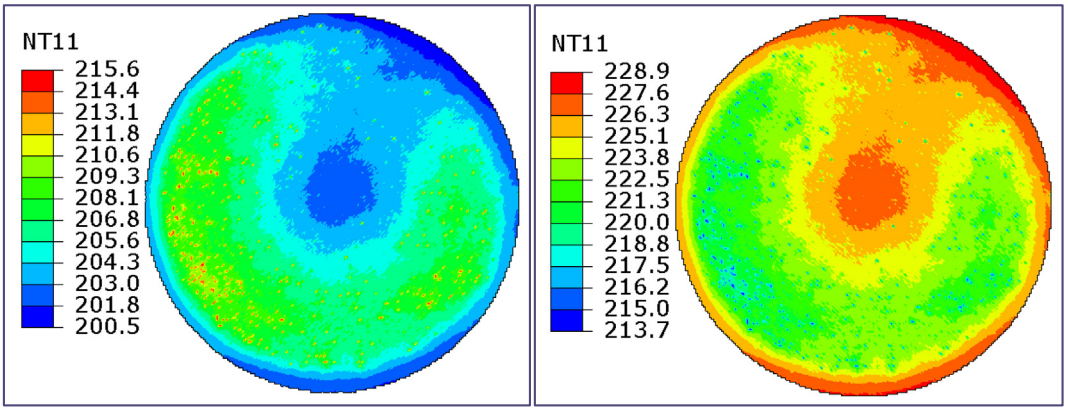

(b1) T_{up}=205.3 ℃ (b2) T_{down}=224.1 ℃

(b)Air

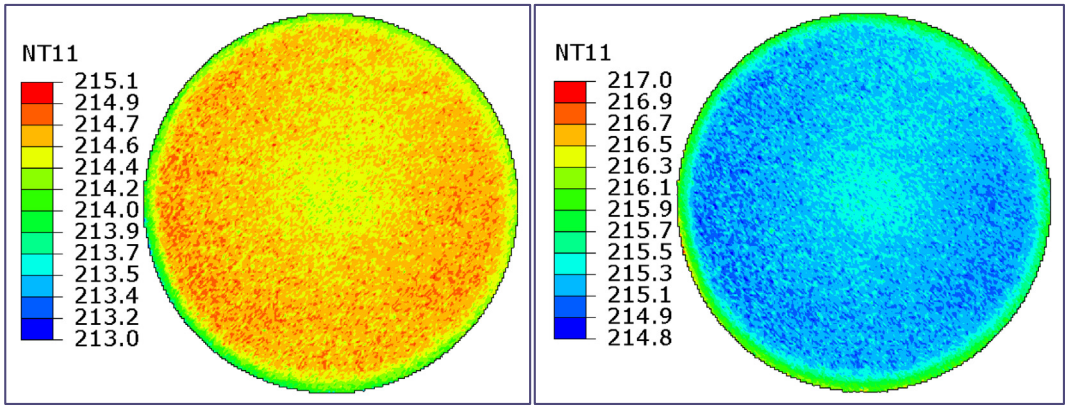

(c1) T_{up}=214.6 ℃ (c2) T_{down}=215.3 ℃

(c)Conductive silicone grease

Fig. 26. Temperature distribution of two contact surfaces (P = 4.65 MPa, Heating temperature 400 °C).

surfaces with air gap is 40169 W/m^2 while that with the vacuum gap is only 16822 W/m^2. So the air conduction contribution is as large as 23347 W/m^2 which is bigger than the solid conduction part. This is ascribed to the reason that the real contact area of the solids is only about 1–2% of the nominal area

4.4.2. Radiation effect

The radiation effect in TCR study is neglected in previous work. In the present study, the effect of radiation for gaps with air and vacuum gap is intensively studied and analyzed. Four conditions of air gap and vacuum gap with or without radiation are numerically simulated. The

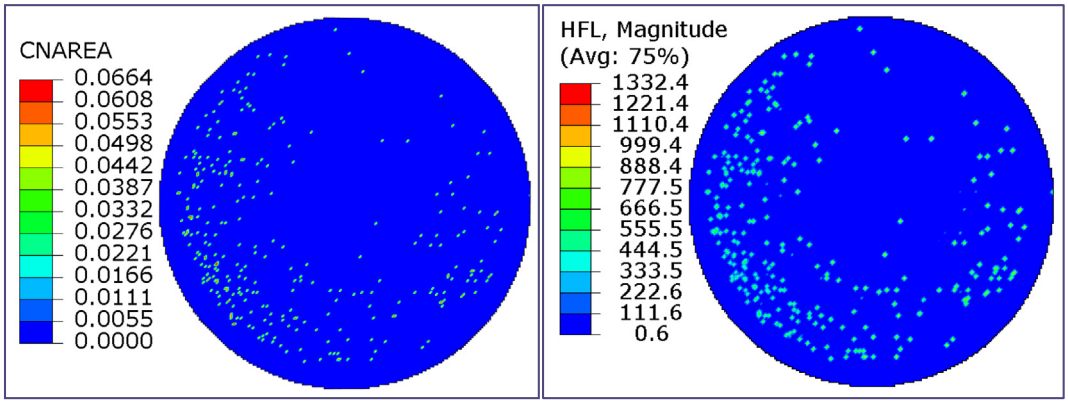

(a)Real contact area (b)Heat flux distribution in vacuum gap

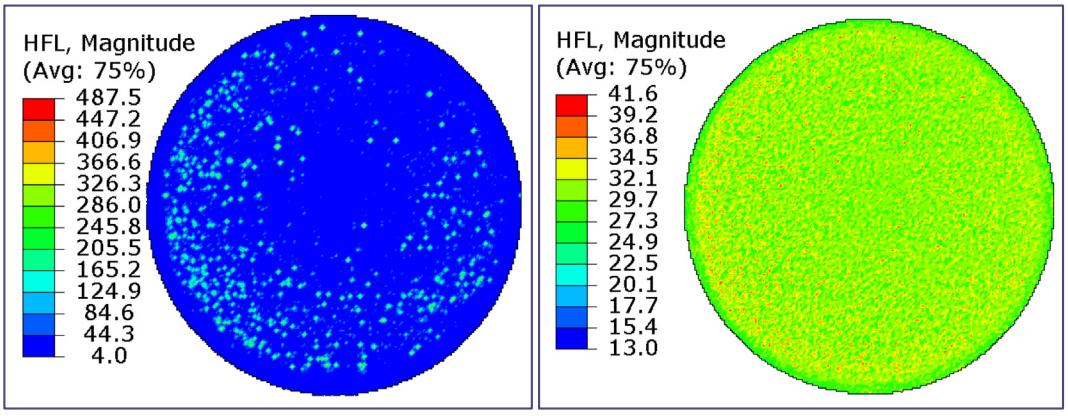

(c) Heat flux distribution in air gap (d) Heat flux distribution in conductive gap

Fig. 27. Heat flux distribution of up-inner-surface of three different interstitial mediums (P = 4.65 MPa, Heating temperature 400 °C).

air gap without radiation is denoted as Condition 1(C1), and the air gap with radiation is denoted as Condition 2(C2). The vacuum gap without radiation is denoted as Condition 3(C3), and the vacuum gap with radiation is denoted as Condition 4(C4). Fig. 29 shows the TCR of air and vacuum gap with and without radiation being considered. The differences are indicated in the two Figures versus the heating temperature under three different loading pressures. TCR decreases with the heating temperature and the loading pressures in both air and vacuum gaps. The difference of TCR with or without radiation increases with the heating temperatures. In particular, the maximum differences of air gap is 2.17%, indicating that when the heating temperature is less than 700 °C the effect of surface radiation on TCR of air gap can be neglected. However, the maximum differences of vacuum gap is nearly 20% within the scope of the study, hence the radiation effect must been taken into account.

4.4.3. Solid thermal conductivities

Supposing that there are three fictitious materials named Material 1, 2 and 3, and they have all the same properties as Ti alloy TC4 except the thermal conductivities. The thermal conductivities are listed in Table 9. Fig. 30 shows the TCR versus the solid thermal conductivity at the loading pressure 12.08 MPa and heating temperature at 500 °C. Results show that TCR rapidly decreases with the solid thermal conductivity. When the thermal conductivity of solid is close to air's at the order of 0.02 $W{\cdot}m^{-1}{\cdot}K^{-1}$, the conduction of solid and gap are both weak leading to a large TCR being at the order of 10^{-3}. When the TC4's thermal conductivity is at the order of 10 $W{\cdot}m^{-1}{\cdot}K^{-1}$, the TCR is at the order of 10^{-4}. And when the solid thermal conductivity is at the order of 400 and 2000 $W{\cdot}m^{-1}{\cdot}K^{-1}$, the conduction of solid is very strong leading to the TCR being at the order of 10^{-5}.

4.5. Correlation

The TCC can be expressed as follows

$$h = c_1 \cdot \left(\frac{\overline{T}}{T_0}\right)^{c_2} \cdot \left(\frac{P}{E_0}\right)^{c_3} \tag{11}$$

where h is the reciprocal of thermal contact resistance (TCR), $W{\cdot}K^{-1}{\cdot}m^{-2}$; T_0 = 293 K, $\overline{T} = \frac{T_{up}+T_{down}}{2}$, °C. P is the loading pressure, MPa; E_0 is the elastic modulus at T_0, 120570 MPa; c_1 = 28740.3 $W{\cdot}m^{-2}{\cdot}K^{-1}$; c_2 = 0.493; c_3 = 0.330. The application range is temperature between 400 °C and 700 °C, pressure between 4.65 MPa and 12.08 MPa; The correlation linear dependency coefficient is 97.8%.

5. Conclusions

This paper proposes a numerical method to predict thermal contact resistance between two solid surfaces based on measuring actual surface topography and using software ABAQUS. A 3-D optical microscope is used to measure the surface topography of contact surfaces. Then contact model is established and the thermal contact resistance simulation is achieved with software ABAQUS for the pair of Ti-6Al-4V—Ti-6Al-4V. The effect of operation conditions (three loading pressures and four heating temperatures) and three kinds of different interstitial material (vacuum, air and conductive silicone grease) are studied and analyzed. The numerical results of thermal contact resistance agree well with the experimental data with the largest deviation 9.57% and 75%

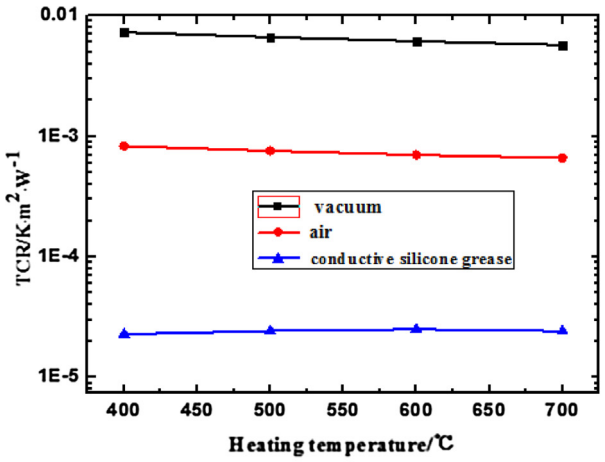

(a) P=4.65 MPa

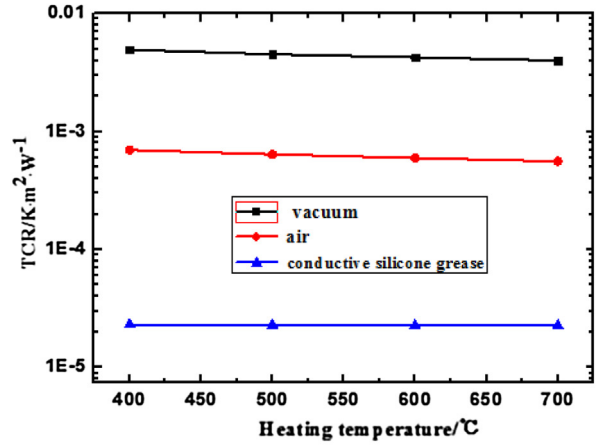

(b) P=7.78 MPa

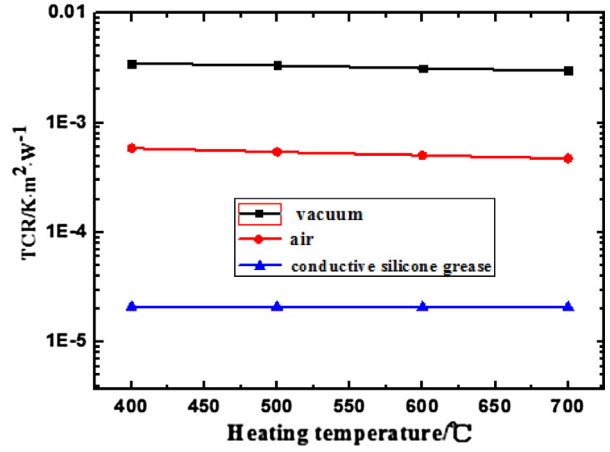

(c) P=12.08 MPa

Fig. 28. The effect of interstitial gap on TCR.

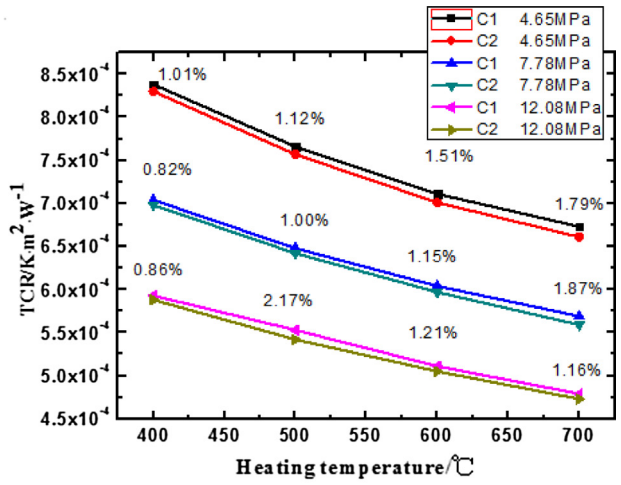

(a) Air gap

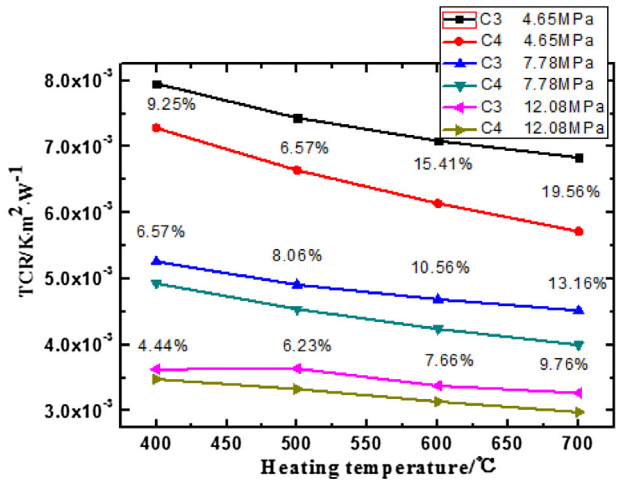

(b) Vacuum gap

Fig. 29. TCR of air and vacuum gap with and without radiation.

deviations within 5%. Following conclusions can be obtained.

(1) This numerical model can be used to predict the thermal contact resistance of micrometer-scale rough surfaces under different temperatures and loading pressures, and different interstitial mediums in case that they can evenly filled in the gap and brings no extra contact resistance between the contact surfaces.
(2) The six major factors to obtain an accurate numerical prediction of the contact thermal resistance by the 1-D steady state model are: (1) The topography of the two contact surfaces should be appropriately presented; (2) The deformation of the contacted points should be accurately determined; (3) The thermal conductivity of the conduction bar should be as accurate as possible. (4) The radiative heat transfer influence on the thermal contact resistance should be considered for high temperature cases under vacuum condition; (5) The thermal conductivity of the material used in the heat transfer model should be temperature dependent; (6) The gap conductance

Table 8
Numerical results of air and vacuum gap with radiation under 7.78 MPa at 600 °C.

Loading pressure(MPa)	Heating temperature (°C)	Condition	T_{up} (°C)	T_{down} (°C)	ΔT (°C)	q (W/m^2)	TCR × 10^4 (K·m^2/W)
7.78	600	C2	318.4	342.4	24.0	40,169	5.97
		C4	294.0	365.4	71.4	16,822	42.4

Table 9
Thermal conductivities of four materials at different temperature.

Thermal conductivity (W/m·K)	Temperature/(°C)	Thermal conductivity (W/m·K)			Temperature/(°C)
Material 1		TC4	Material 2	Material 3	
0.02	20	7.4	393	2000	100
0.022	200	8.7	389	2000	200
0.024	400	9.8	384	2000	300
0.029	600	10.3	379	2000	400

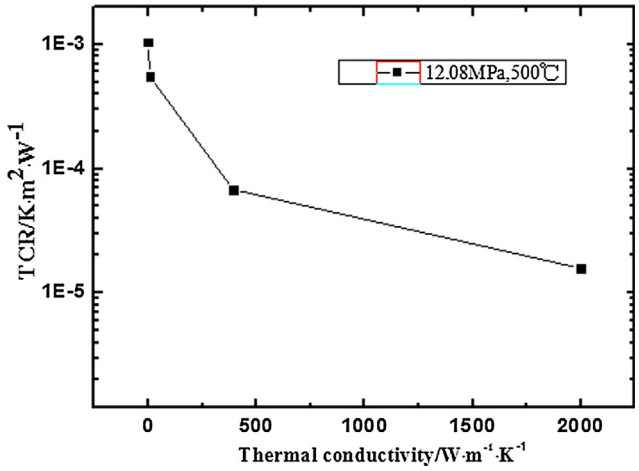

Fig. 30. The effect of solid thermal conductivity on TCR.

should be given with the individual gap conductance instead of an empirical parameter contact conductance.

(3) The thermal contact resistance of Ti-6Al-4V—Ti-6Al-4V decreases with the loading pressures and heating temperatures.

(4) Below the heating temperature of 700 °C, the radiation effect on thermal contact resistance of air gap can be neglected while it has relatively large effect on the thermal contact resistance of vacuum gap.

(5) Both the solid and interstitial medium thermal conductivity have significant effect on the thermal contact resistance. The thermal contact resistance decreases with the solid and interstitial gap thermal conductivity. The thermal contact resistance of vacuum gap is 10 times larger than that of air gap while the thermal contact resistance of air gap is 50 times larger than that of grease gap under the same boundary conditions.

(6) The correlation can be expressed as $h = c_1 \cdot \left(\frac{\bar{T}}{T_0}\right)^{c_2} \cdot \left(\frac{P}{E_0}\right)^{c_3}$.

Acknowledgment

This study is supported by the Key Project of International Joint Research of National Nature Science Foundation of China (51320105004), China Postdoctoral Science Foundation (2017M623166) and the 111 Project (B16038).

References

[1] Wang AL, Zhao JF. Review of prediction for thermal contact resistance. Sci China: Technol Sci 2010;53(7):1798–808.
[2] Cohen A, Watwe AA, Prasher RS. Heat transfer in electronic equipment. In: Bejan A, Kraus AD, editors. Heat transfer handbook. New York: John Wiley; 2003. p. 947–1027.
[3] Dean RA. Thermal contact conductance between UO_2 and Zircaloy-2 Report CVNA-127 Pittsburgh (PA): Westinghouse Electric Corporation; 1962
[4] Snaith B, O'Callaghan PW, Probert SD. Interstitial materials for controlling thermal conductances across pressed metallic contacts. Appl Energy 1984;16(3):175–91.
[5] ASTM D5470-06. Standard test method for thermal transmission properties of thermally conductive electrical insulation materials. America: ASTM International; 2006.
[6] Madhusudana CV. Accuracy in thermal contact conductance experiments – the effect of heat losses to the surroundings. Int Com Heat Mass Transf 2000;27(6):877–91.
[7] Ding C, Wang R. Thermal contact conductance of stainless steel-GFRP interface under vacuum environment. Exp Therm Fluid Sci 2012;42:1–5.
[8] Zhang P, Xuan Y, Li Q. A high-precision instrumentation of measuring thermal contact resistance using reversible heat flux. Exp Therm Fluid Sci 2014;54:204–11.
[9] Liu D, Luo Y, Shang X. Experimental investigation of high temperature thermal contact resistance between high thermal conductivity C/C material and Inconel 600. Int. J. Heat Mass Transfer 2015;80:407–10.
[10] Choi YS, Kim MS. Experiments on thermal contact conductance between metals below 100K. AIP Conf Proc 2014;1573:1070–7.
[11] Yovanovich MM. Four decades of research on thermal contact, gap, and joint resistance in microelectronics. IEEE Trans Compon Packag Technol 2005;28(2):182–206.
[12] Bakolas V. Numerical generation of arbitrarily oriented non-gaussian three-dimensional rough surfaces. Wear 2003;254(5–6):546–54.
[13] Zou MQ, Yu BM, Cai JC, et al. Fractal model for thermal contact conductance. J Heat Transf 2008;130(10). 101301-1–101301-9.
[14] Pennec F, Peyrou D, Leray D, et al. Impact of the surface roughness description on the electrical contact resistance of ohmic switches under low actuation forces. IEEE Trans Compon Packag Manuf Technol 2012;2(1):85–94.
[15] Mikic BB. Thermal contact conductance: theoretical considerations. Int J Heat Mass Transf 1974;17:205–14.
[16] Cooper MG, Mikic BB, Yovanovich MM. Thermal contact conductance. Int J Heat Mass Transf 1969;12:279–300.
[17] Yovanovich MM. Thermal contact correlations. In: AIAA 16th thermophysics conference, Palo Alto, California, USA; 1981. p. 83–95.
[18] Bush AW, Gibson RD. A theoretical investigation of thermal contact conductance. Appl Energy 1979;5(1):11–22.
[19] Sridhar MR, Yovanovich MM. Elastoplastic contact conductance model for isotropic conforming rough surfaces and comparison with experiments. Trans AMSE J Heat Transf 1996;118:3–9.
[20] Cui TF, Li Q, Xuan YM, Zhang P. Multiscale simulation of thermal contact resistance in electronic packaging. Int J Therm Sci 2014;83:16–24.
[21] Verma NN, Mazumder S. Extraction of thermal contact conductance of metal–metal contacts from scale-resolved direct numerical simulation. Int J Heat Mass Transf 2016;94:164–73.
[22] Murashov MV, Panin SD. Numerical modelling of contact heat transfer problem with work hardened rough surfaces. Int J Heat Mass Transf 2015;90:72–80.
[23] Thompson MK. A multi-scale iterative approach for finite element modelling of thermal contact resistance. Cambridge (MA, USA): Massachusetts Institute of Technology; 2007.
[24] Gou JJ, Ren XJ, Dai YJ, Li S, Tao WQ. Study of thermal contact resistance of rough surfaces based on the practical topography. Comput Fluids 2016.
[25] Lee OJ, Lee KH, Yim TJ, et al. Determination of mesopore size of aerogels from thermal conductivity measurements. J Non-Cryst Solids 2002;298:287–92.
[26] DS.SIMULIA.ABAQUS.2016.0.DOCS.
[27] Bowden FP, Tabor D. The friction and lubrication of solids. London: Oxford University Press; 2001. p. 20–32.